

Geologic Storage of CO₂

*GCEP Annual Report
May 7, 2007*

Section 4: Dynamic Imaging for Seismic Monitoring of CO₂ Storage in Coal

<i>Introduction.....</i>	<i>53</i>
<i>Review of Field Seismic Studies for Coal</i>	<i>55</i>
<i>Configurations for Seismic Monitoring</i>	<i>56</i>
<i>Diffraction Tomography Filters for Studying Acquisition Geometries</i>	<i>59</i>
<i>Imaging with Feature-enhanced Adaptive Meshes and Temporal Regularization</i>	<i>61</i>
<i>Data Evolution and Model Evolution</i>	<i>65</i>
<i>Summary</i>	<i>69</i>
<i>Future Work.....</i>	<i>70</i>
<i>References.....</i>	<i>70</i>

4. Dynamic Imaging for Seismic Monitoring of CO₂ Storage in Coal

Introduction

Flow simulation is used to predict the flow and storage of CO₂ in coalbeds. However, the behavior of injected CO₂ is not fully predicable because sites are never fully described, and in situ processes are not fully understood. Therefore, we will need to monitor the storage during and after the injection. When compared with other geological settings, e.g. depleted oil and gas reservoirs and deep saline aquifers, coalbeds present special challenges and features to exploit in monitoring. Figure 39 captures the monitoring workflow and shows the research activities on monitoring. It also shows the relationship between the monitoring activities. CO₂ flow simulation, the DARS laboratory measurements. The monitoring research is a simulation study involving the creation of proper time-lapse seismic models from flow simulations and two paths of image simulation: (A) Simulations that capture as best we know the physics of wave propagation in visco-elastic media and the subsequent space-time imaging/inversion process; (B) Simulations that yield idealized seismic images (perhaps 100's) extremely fast for testing acquisition configurations and temporal integration.

The goal of this approach is to develop a seismic imaging method that recursively constructs time-lapse subsurface images of CO₂ from continuously recorded data. We call this “dynamic subsurface monitoring” because it must exploit the temporal integration of measurements, knowledge of the changes in coals due to injected CO₂, and model predictions from flow simulations or other sources. This dynamic imaging concept builds from the high-resolution baseline survey that is recorded for purposes of site selection and site characterization. To this baseline dataset, we propose to add small increments of data and perform lower-resolution reconnaissance imaging on a quasi-continuous basis. Should a reconnaissance image indicate a problem with CO₂ containment, acquisition resources are deployed to implement a high-resolution survey targeted on the problem area. Due to the relatively shallow nature of coalbeds, we exploit integrated source-detector geometries that might be considered impractical for deeper petroleum reservoirs or deep aquifers. This research is divided into two closely related tasks: (1) dynamic time-lapse imaging from sparse datasets; and (2) feature-enhanced model parameterization.

A diagram for the data flow of dynamic imaging is shown in Figure 40. This approach applies traditional tomography as follows: (1) Data are recorded with source-detector geometries (embedded for repeatability) from sources and detectors at the surface and in shallow slim boreholes. This geometry allows any combination of surface-to-surface profiles, quasi-vertical profiles, and quasi-crosswell profiles; (2) smart parameterization wherein a spatially variable mesh is used in the inversion to parameterize model updates, i.e., fewer unknowns in sections not expected to change and more unknowns in areas where changes are anticipated. The variable mesh is derived from flow predictions and temporal model history; (3) model evolution is used to assist development of the spatial mesh in order to reduce the number of spatial parameters in the update model; (4) data evolution is used to reduce the number of new samples needed in the time-lapse data volume. Data evolution complements the sparse data recordings by

filling out the data array with estimates predicted from data history. A simplistic approach to data evolution is to replace old data by zipping new data into the previous dataset. A better approach is to use a Kalman filter or other processing algorithm to predict data. Each component of this model plays an important role in the development of quality images from sparse datasets. The generic term tomography is used here to describe the process of imaging, and can be implemented from any source-detector geometry for transmitted, reflected, or diffracted wave events or any combination of these events.

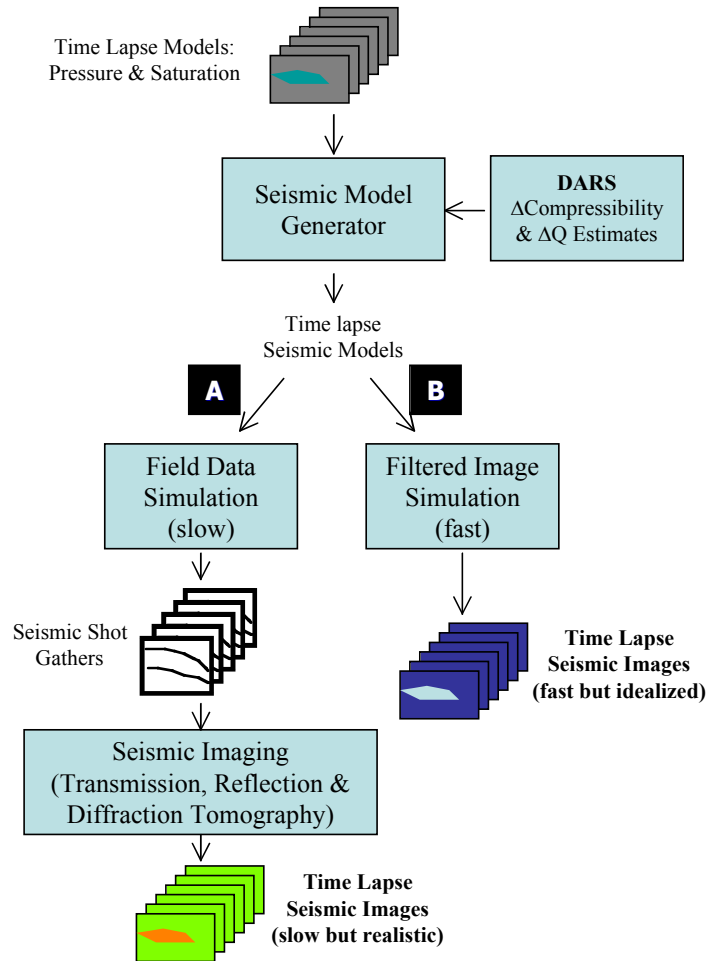


Figure 39: Workflow for the CO₂ monitoring studies. Flow simulation provides a series of pressure and saturation models corresponding to different times during CO₂ injection. The pressure and saturation changes are then converted into seismic property models with help from laboratory measurements of rock properties. Two paths are implemented for simulating the seismic images; (A) the expensive and slow process of simulating data acquisition and imaging; (B) an inexpensive and fast process of generating idealized seismic image.

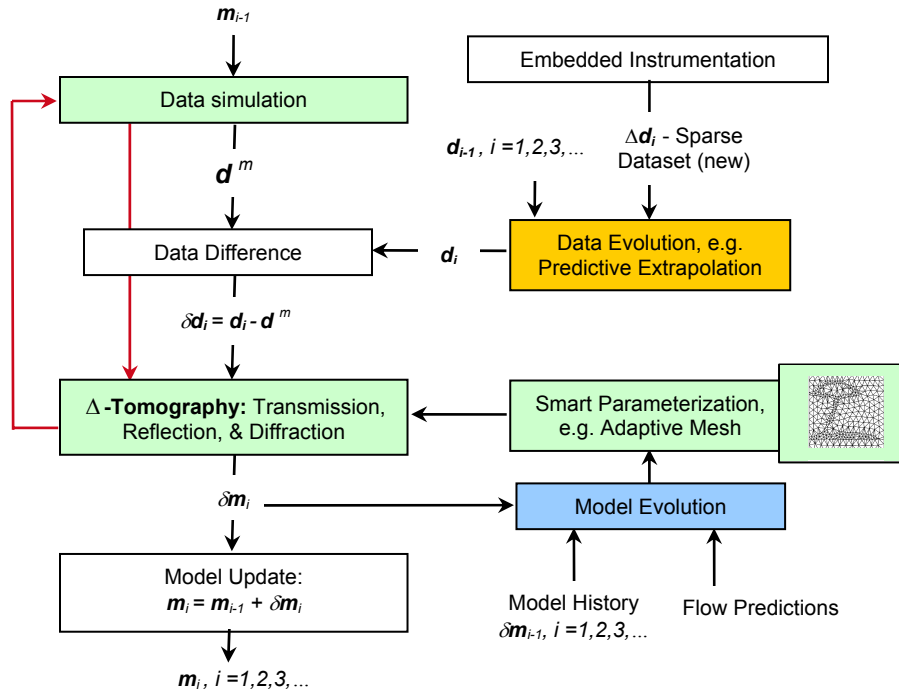


Figure 40: The data processing flow for dynamic subsurface monitoring combines elements of feature-enhanced parameterization and imaging from sparse datasets.

Review of Field Seismic Studies for Coal

A literature review on coal seismic field studies is helpful for us to develop new seismic monitoring methods for coalbeds. Seismic methods have been extensively used for coal mine characterization and fault evaluation [1, 3, 4, 5, 6, 7, 8, 10], though not as much as in the oil and gas industry. Those coal surveys included 3-D high resolution seismic, vertical seismic profiling (VSP), crosswell seismic profiling, and sonic logging. Coals have low densities and low seismic wave velocities, typically *in situ* P -wave velocities in a range of 2–3 km/s. Coalbeds usually have large contrast against surrounding rocks, and as a result strong guided waves may exist in a coal layer. Figure 41 shows a typical P -wave velocity profile adapted from [8], which will be used for some modeling later in this report. Coalbeds of interest tend to be relatively shallow, with depths less than about 1000 m. Coals typically have high attenuation (or low Q -values); the *in situ* measurement of Q -value given in [3] is about 45. Coalbeds may have strong anisotropy [3] due to aligned fractures and micro layering. Lab measurements on coal samples show as much as 40% P -wave anisotropy [2].

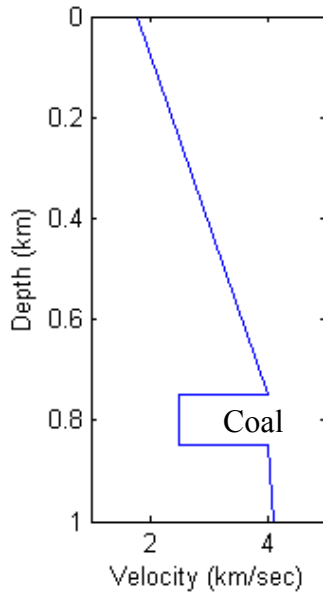


Figure 41: A *P*-wave velocity profile adapted from[8] from a coal mine.

Configurations for Seismic Monitoring

We are proposing a special configuration of seismic sources and detectors system suitable for monitoring of CO₂ storage in coal, or other shallow subsurface monitoring projects. Figure 42 shows a diagram of this 3-D configuration implemented with embedded instrumentation. Circular array(s) on the surface acquires surface reflection data. Vertical arrays are located in near surface boreholes. Optionally, a deep array is embedded near the storage zone in the injection borehole. If we assume the target to be at a depth d which is relatively shallow, the vertical array is 20% or less of d (~200 m). We use the 20% vertical array to demonstrate that the slim instrumentation boreholes should be affordable. The optimum length of the vertical array has yet to be determined. If the length is too long, they will cost too much and also could penetrate the storage area possibly creating risks to CO₂ leaks. If the array length is too short, the aperture would be too small to improve imaging of the target. The applications of vertical arrays for seismic data acquisition can be found in [11, 12, 13].

This configuration can record reflection and refraction data from several different source-detector configurations. We show in Figure 42 only one circular array along with six vertical arrays near the surface. In fact, we can adaptively expand the diameter of the circular array or place as many additional vertical arrays as needed to improve coverage the volume. Using the velocity model shown in Figure 41, we have calculated the ray paths for different survey geometries and will discuss these below. In the case of enhanced coal bed methane (ECBM), CO₂ replaces CH₄. In this multi-component case, the injected CO₂ may not cause detectable velocity changes but may have detectable attenuation changes. In this situation, passive seismic monitoring may be an effective method because it detects induced seismicity associated with pressure and fluid flow

front. The proposed acquisition configuration provides good coverage for passive microseismic observations as well as active seismic imaging, though passive seismic monitoring is not part of this project.

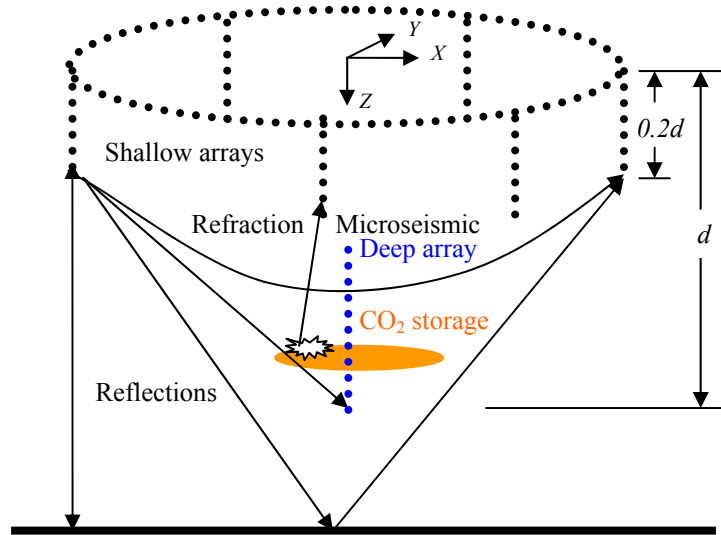


Figure 42: Source-detector configuration for seismic monitoring of shallow coalbeds.

Figure 43 illustrates ray paths of transmitted-refracted waves recorded with the vertical arrays. The near surface velocity gradient makes it possible to detect velocity changes below the transducers. Moreover, the length of the vertical array provides an aperture to improve imaging of the volume below. The penetration depth of the refraction wave depends on the velocity gradient and the horizontal separation of the vertical arrays. Although these waves may not penetrate the storage region of the coalbed, they will provide seismic surveillance above the coal and in the near subsurface for any upwelling CO₂ in the event of a leak. Although the circular array records traditional surface reflection data, these near surface vertical arrays can also record reflections as displayed in Figure 43a. The reflections come from above and below the coal boundaries. In comparison with transmitted-refraction tomography in Fig 43a, reflections of the type shown in Fig. 43b have higher vertical resolution. Using both refraction and reflection data improves resolution and coverage of the subsurface.

The third option is to place a deep detector array behind casing of the injection well to further improve image resolution and coverage without significantly increasing cost. This configuration is a vertical seismic profile or VSP, for which typical reflection raypaths are shown in Figure 43c. Strong transmitted waves (not shown) from sources in the vertical arrays are also useful for velocity estimation and amplitude calibration.

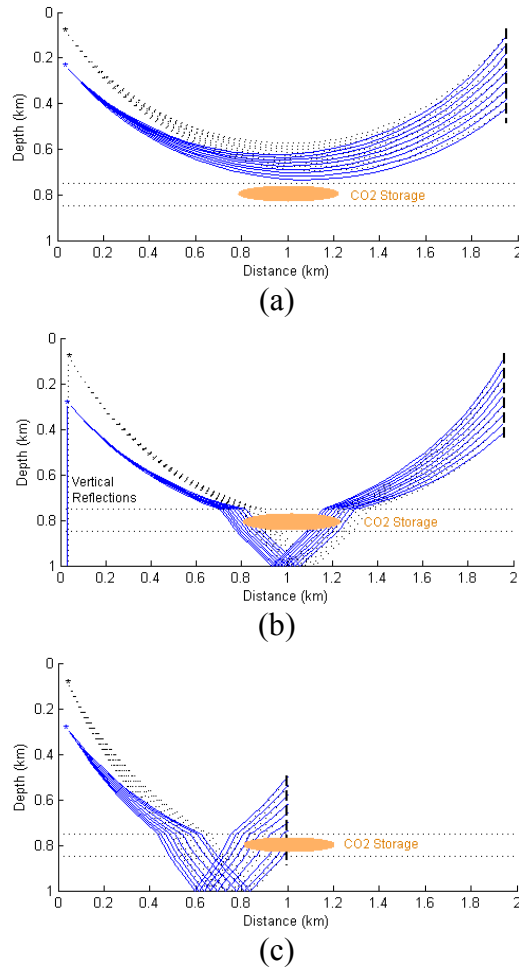


Figure 43: Typical raypaths recorded from vertical arrays: (a) Transmitted-refraction waves; (b) Reflected-refraction waves; (c) VSP reflected-refracted waves.

The types of images we can construct with these configurations of source and detectors are summarized in Table 4.1. As mentioned above, the design of this configuration is directed towards the relatively shallow subsurface targets of coalbed storage. In the case of deep targets, the length of the embedded vertical arrays and the diameter of the circular array would not be large enough to provide adequate imaging apertures.

Table XII: Possible image reconstructions with data from the various arrays.

	Transmission Tomography	Reflection Tomography	Diffraction Imaging
Circular surface array(s)		X	X
Shallow vertical arrays	X	X	X
Deep borehole array	X	X	X

Diffraction Tomography Filters for Studying Acquisition Geometries

In order to test the various strategies for quasi-continuous monitoring, we require a modeling technique that is capable of modeling hundreds of time—sequential models, produced say from a flow simulator. The three “rigorous” steps of a modeling procedure are: (1) generate a synthetic seismic dataset by simulating every source and detector location for each time-lapse model; (2) processing each dataset to separate the wavefield event to be used in imaging; (3) invert each dataset for the time-lapse image. This procedure, as outlined above, is much too slow and expensive to perform on the numerous models that come from the flow simulator. Moreover, we may need to repeat the steps many times for the same model as we test various acquisition geometries. In this subsection, we describe a fast method of simulating the ideal seismic image resulting from a specific data acquisition geometry for a given geo-flow model. This fast image simulation method (path B in Figure 39) applies multi-dimensional spatial filters to the geo-flow model to generate the image. The results of this study helps to understand the seismic imaging with a hybrid combination of surface and vertical arrays. Studying these acquisition geometries described above for advantages and disadvantages under various conditions of CO₂ storage. This spatial filter approach comes from diffraction tomography [29, 20]:

$$O(x, z) = \frac{1}{(2\pi)^2} \iint \tilde{O}(K_x, K_z) \exp[i(K_x x + K_z z)] dK_x dK_z,$$

where $\tilde{O}(K_x, K_z)$ is the filtered spatial Fourier transform of the model, $\mathbf{K} = (K_x, K_z)$ is the spatial frequency vector constructed from the source-detector geometry, and $O(x, z)$ is the reconstruction of the model as viewed through this seismic filter. Different acquisition geometries and signal properties yield different filters of the earth model. Figure 44a shows the “full aperture” spectral coverage for surface reflection profiles (SRP), crosswell seismic profiles (XSP) and vertical seismic profiles (VSP) acquisition geometries at the same frequency. It can be seen that the range of spatial frequencies covered is incomplete with either geometry, which means the inverted model will not yield a perfectly reconstructed image. Because more than one frequency is used in field experiments and the acquisition apertures are less than 180°, it is noteworthy to show the more realistic limited aperture multi-frequency filters (Figure 44b).

To illustrate the utility of this approach we manually created 221 time-lapse models. (We are working on the creation of these kinds of leaky models using a coal flow simulator). The first one (M₀) is the baseline model. CO₂ is injected near the bottom right side. We assume that CO₂ saturation reduces the velocity. The filters used are shown in Figure 45. The frequency ranges for the three geometries are different: 1-50 Hz, 700-1000 Hz, and 1-150 Hz for SRP, XSP, and VSP, respectively.

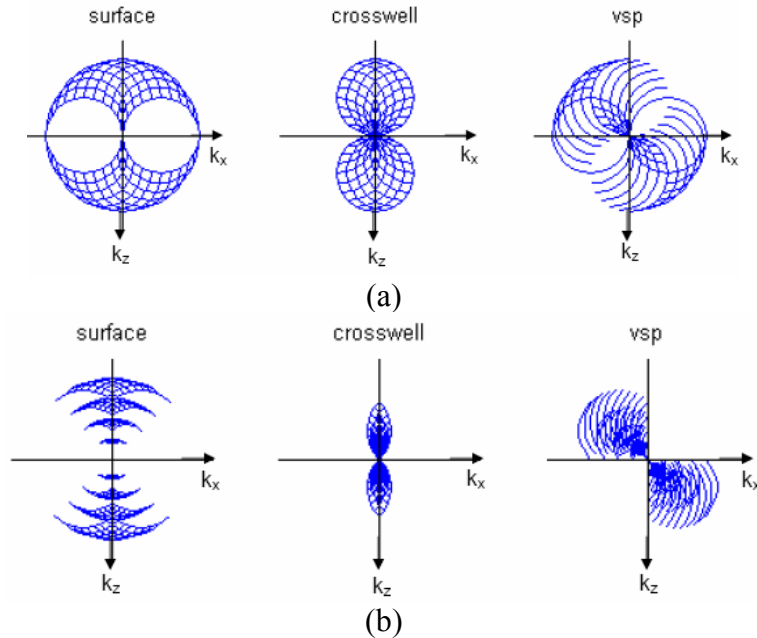


Figure 44: The single-frequency spatial filters obtained for 3 geometries from (a) full 180° apertures; (b) more realistic “limited apertures” with 90° maximum angular range.

The models are shown along the top row of Figure 46 and the SRP images for these models in the second row. The “true” model differences are presented in the third row of Figure 46 and the difference images for the SRP geometry in the fourth row. Finally, we show the XSP and VSP images in the lower two rows. Starting from Model 120 (M_{120}), an upward leak can be seen to develop and create a thin vertical feature. The seismic images fail to capture this leak because of poor coverage in the lateral direction for the SRP and XSP geometries as can be seen from the absence of K_x samples in the filters shown in Figure 45. The VSP geometry has better K_x coverage and its reconstructed image resolves this small vertical feature best. This idealized image simulation approach shows how different acquisition geometries sample the Fourier components of the model. It can produce ideally-reconstructed images in minutes for hundreds of time-lapse models, in contrast to path A in figure 39 that would take months to simulate.

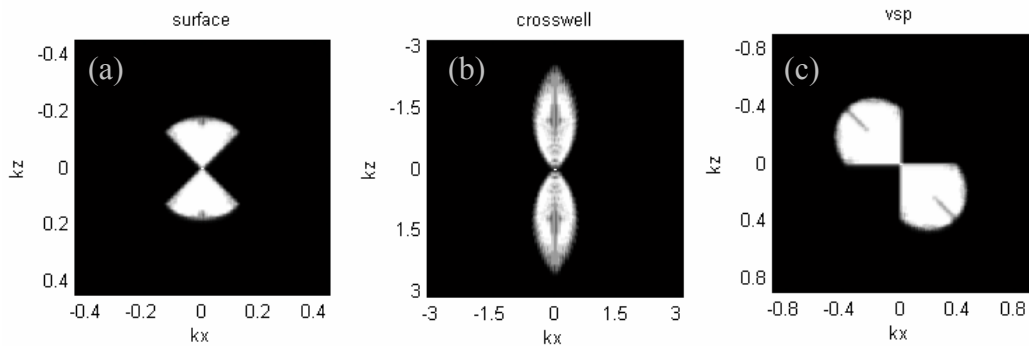


Figure 45: Spatial frequency filters used in the filtered image models (Fig 46).

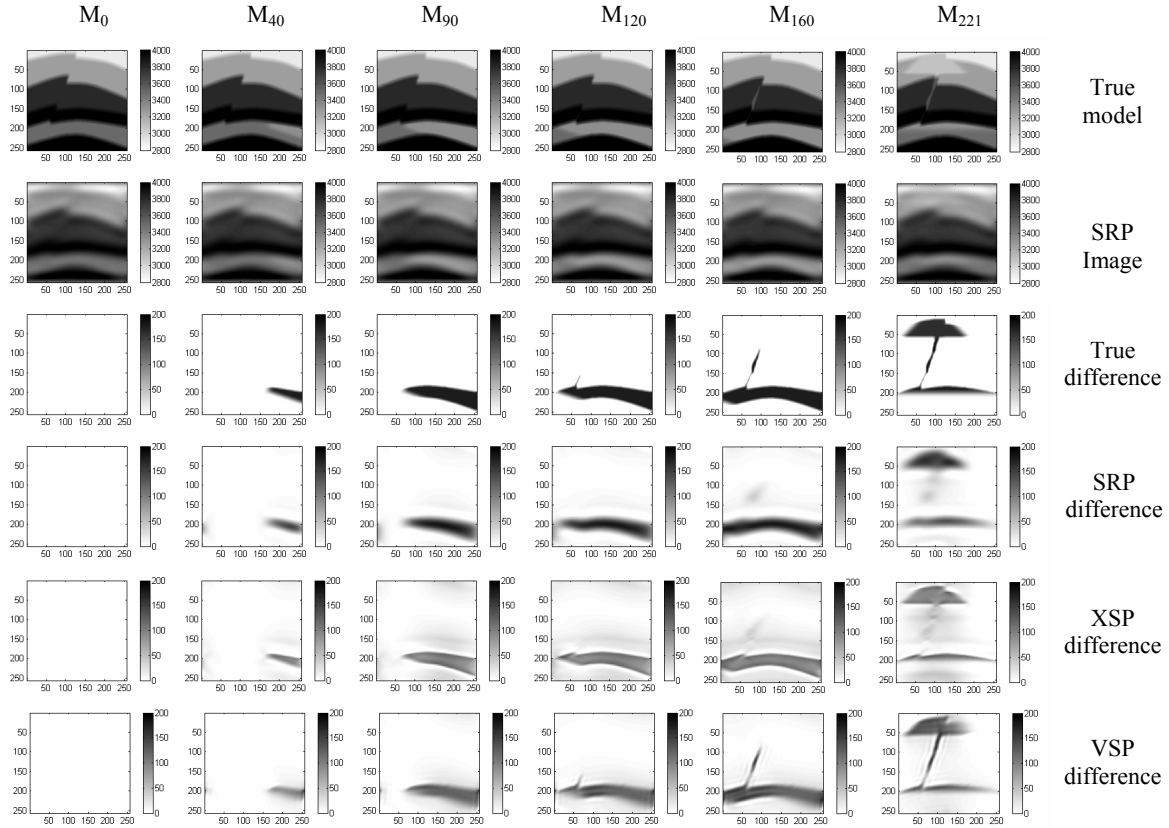


Figure 46: Filtered diffraction tomography for surface seismic reflection profiles (SRP), crosswell seismic profiles (XSP) and vertical seismic profiles (VSP).

We will use this fast simulation tool to address fundamental questions on optimal acquisition geometries, advantages and disadvantages of combined arrays, and test of the temporal integral loop.

Imaging with Feature-enhanced Adaptive Meshes and Temporal Regularization

The expected subsurface changes are expected to occur in localized regions due to CO₂ and pressure. The geology changes little if any. Conventional imaging approaches often estimate many more parameters than needed because these main structural features do not change. This results in image artifacts from computing differences between surveys due to different successive estimations of these static geological structures [25]. In order to minimize such undesirable effects, we propose a temporal integration technique combined with a reduction in the number of model parameters to be estimated. Temporal integration is accomplished through joint inversion of incremental new data with data from previous surveys. New data are more strongly related with current subsurface models and therefore should have heavier weights in this joint inversion.

Reduction in the number of parameters is achieved by feature-enhanced adaptive meshing. One of the advantages of the adaptive triangular mesh [14] is the resolution achieved through use of a finer mesh near the front of the injected CO₂ plume. Another advantage is the implicit spatial regularization that occurs due to the use of coarser meshes in slow-varying regions. Thus, we use adaptive triangular adaptive meshes, temporal integration and spatial regularization [28] for the time-lapse imaging. Moreover, the triangular mesh is used to reduce the number of model parameters. However, we also want to keep the simple formulation of the tomographic matrix and regularization for conventional regular grids. Thus, we derived a different formulation for the use of triangular meshes that allows mapping between triangle vertexes and a regular grid. This approach can be used as a general framework to solve linear inverse problems for different areas using triangles instead of cells as basic elements, with minimal impact to original problem formulation. The key concept is to describe each cell of a regular grid as a linear combination of control nodes values at triangle vertexes, considering the respective triangle that covers each region of regular grid. Thus, a linear operator T may be explicitly defined to map any regular grid into control nodes of a triangular mesh. This approach also keeps the possibility of using its inverse mapping T^{-1} to find a regular (or rectangular) grid representation from a triangular representation, which is useful to display the resulting image of tomographic inversion.

The algorithm that computes matrix T has the following steps for each triangle of mesh: (1) Identify its three vertexes to compute vertex weights based on relative position of interior cells of the triangle; (2) compute weights for each cell of regular grid within current triangle using barycentric coordinates interpolation; (3) store these weights into a matrix T that maps each cell value as a linear combination of control nodes triangle vertexes. The interpolation using barycentric coordinates is based on the areas of three imaginary triangles formed by lines between triangle vertexes and an interior point [17]. These three areas are used as a measurement of influence of each control node vertex onto a point belonging to a triangular mesh element, resulting in three respective weights for each interior point. Considering v_1 , v_2 and v_3 as the control values at respective positions \mathbf{r}_1 , \mathbf{r}_2 and \mathbf{r}_3 corresponding to vertexes of each triangle, the weights for each interior point at position \mathbf{r} are given by the following expressions:

$$w_1(\mathbf{r}) = \frac{(\mathbf{r} - \mathbf{r}_2) \times (\mathbf{r}_3 - \mathbf{r}_2) \cdot \mathbf{e}_3}{(\mathbf{r}_1 - \mathbf{r}_2) \times (\mathbf{r}_3 - \mathbf{r}_2) \cdot \mathbf{e}_3},$$

$$w_2(\mathbf{r}) = \frac{(\mathbf{r} - \mathbf{r}_1) \times (\mathbf{r}_3 - \mathbf{r}_1) \cdot \mathbf{e}_3}{(\mathbf{r}_2 - \mathbf{r}_1) \times (\mathbf{r}_3 - \mathbf{r}_1) \cdot \mathbf{e}_3},$$

$$w_3(\mathbf{r}) = \frac{(\mathbf{r} - \mathbf{r}_1) \times (\mathbf{r}_2 - \mathbf{r}_1) \cdot \mathbf{e}_3}{(\mathbf{r}_3 - \mathbf{r}_1) \times (\mathbf{r}_2 - \mathbf{r}_1) \cdot \mathbf{e}_3},$$

where \mathbf{e}_3 is the unitary vector (0,0,1). This leads to the following expression that maps nodes control values from triangular mesh into a regular grid cell value $o(\mathbf{r})$ for each triangle:

$$o(\mathbf{r}) = \sum_{i=1}^3 w_i(\mathbf{r})v_i(\mathbf{r}).$$

The matrix T performs this mapping for each cell of regular grid using respective triangles that covers its different regions. Thus, nodes control values at triangle vertexes are mapped into a regular grid using the forward mapping expression $\mathbf{o} = T\mathbf{v}$ and the inverse mapping from regular grid into control nodes values of triangular mesh is given by $\mathbf{v} = T^{-1}\mathbf{o}$. This allows a straightforward modification to convert a regular grid method into a triangular mesh method. From a simple regular grid formulation for linear problems $\mathbf{p} = W\mathbf{o}$, where \mathbf{p} is the data vector and \mathbf{o} is the model parameter vector, one may use the expression for triangular meshes $\mathbf{p} = WT\mathbf{v}$. For linear inverse problems, this expression may be applied to estimate triangular mesh control node values from data vector

$$\mathbf{v} = (WT)^+ \mathbf{p},$$

where the superscripted plus symbol means pseudo-inverse [23] computed using SVD. An equivalent regularized system may also be obtained from

$$\begin{bmatrix} W \\ \lambda D \end{bmatrix} T\mathbf{v} = \begin{bmatrix} \mathbf{p} \\ \mathbf{0} \end{bmatrix},$$

where D is a numerical derivative matrix and λ is a constant [27]. After parameter estimation, the resulting triangular mesh control values can be easily displayed as a regular grid using forward mapping of linear operator T , as described earlier.

The second component this scheme is time regularization. Time-lapse imaging conventionally inverses different data sets independently and then analyzes image subtraction to identify changes. This straightforward approach repetitively estimates fixed geology structures as well model changes due to pressure and saturation, ignoring the similarities between successive images that could be useful during inversion. A smarter approach uses a temporal derivative operator to integrate data along time using previous information combined with repeated surveys [16]. It requires solving an integrated linear system that contains previous survey equations and temporal derivative equations minimization. We adopted a different approach that integrates previous surveys information but uses a scalar factor to damp the influence of each previous survey into the latest survey information available by forming an augmented system

$$\begin{bmatrix} W_k \\ \alpha_{k-1}W_{k-1} \\ \vdots \\ \alpha_{k-ns+1}W_{k-ns+1} \end{bmatrix} \mathbf{o} = \begin{bmatrix} \mathbf{p}_k \\ \alpha_{k-1}\mathbf{p}_{k-1} \\ \vdots \\ \alpha_{k-ns+1}\mathbf{p}_{k-ns+1} \end{bmatrix},$$

where index k represents the newest survey, ns is the number of available surveys and α_{k-i} is a normalized scalar proportional to the influence of earlier survey $k-i$ into current inversion, being smaller for older surveys. Since relevant information from previous surveys is included in this equivalent system, a new smaller and less expensive survey

may be performed to update subsurface image. This procedure can be repeated for newer datasets and keeps relevant information from previous ones, increasing the number of rows by the number of newer survey equations but keeping fixed the number of columns of equivalent linear system, which may not occur when using temporal derivative operator approaches.

The imaging method with triangular mesh and temporal integration discussed above can be used for relatively general linear geophysical inversion. We now apply it to seismic diffraction tomography [29, 20], where the incident field from a source at \mathbf{r}_s can be represented through the Green's function $G(\mathbf{r}_s | \mathbf{r}')$ and the scattered field at receiver \mathbf{r}_g can be calculated by

$$P_s(\mathbf{r}_s, \mathbf{r}_g) = -k_0^2 \int O(\mathbf{r}') G(\mathbf{r}' | \mathbf{r}_s) G(\mathbf{r}_g | \mathbf{r}') d\mathbf{r}' .$$

This formula is the space domain forward modeling equivalent to the diffraction tomography formula used above to create the fast filter image simulator. Discretization of the above equation leads to the linear system $\mathbf{p} = W\mathbf{o}$, which has to be inverted in order to recover $O(\mathbf{r})$ [26]. In this work the inversion was done using SVD, but could be done using other linear system solvers.

Next, we simulate a CO₂ monitoring experiment to test this time regularization algorithm. As discussed above, we have 221 time-lapse CO₂ flooding models. Five of these time-lapse models are presented in Figure 47 for the VSP geometry. The figures show only the velocity difference compared with the background medium (~4,000 m/s). There is a negative velocity contrast (2%) caused by CO₂ injection. Data are simulated for each model for 28 sources and 28 receivers. Triangular adaptive meshes (column b) are generated based on velocity gradient from *a priori* information, leading to the inversion results shown in column c. A regular grid would provide good results for this base survey as well, since a reasonable number of sources and receivers are employed. As discussed above, *a priori* information from reservoir flow simulation or from previous surveys may be used to generate adaptive meshes. The adaptive mesh inversion reduces the number of parameters but maintains robustness, since triangles at slow-varying velocity fields regions are coarser but still useful to perform good imaging even with low quality *a priori* information. Since the previous datasets is integrated into inversion, the successive updates use a fewer and consequently less expensive datasets. In our example, we use a constant scalar for the immediately previous survey $\alpha = 0.3$ and adopt respectively α^2 , α^3 and so on when other earlier surveys were available and evenly sampled along time. We apply spatial regularization for order 2 and $\lambda = 0.02$ for all inversions. A naive regular grid inversion for such image resolution would require 50 sources and 50 receivers for each time-lapse inversion, which means that it would require three times more data measurements than we used here. This reduction in the number of parameters is reinforced by temporal integration of previous survey to achieve current subsurface image. Thus, problems that are originally underdetermined can be reformulated as overdetermined without the drastic decrease of resolution required for regular grids under similar circumstances.

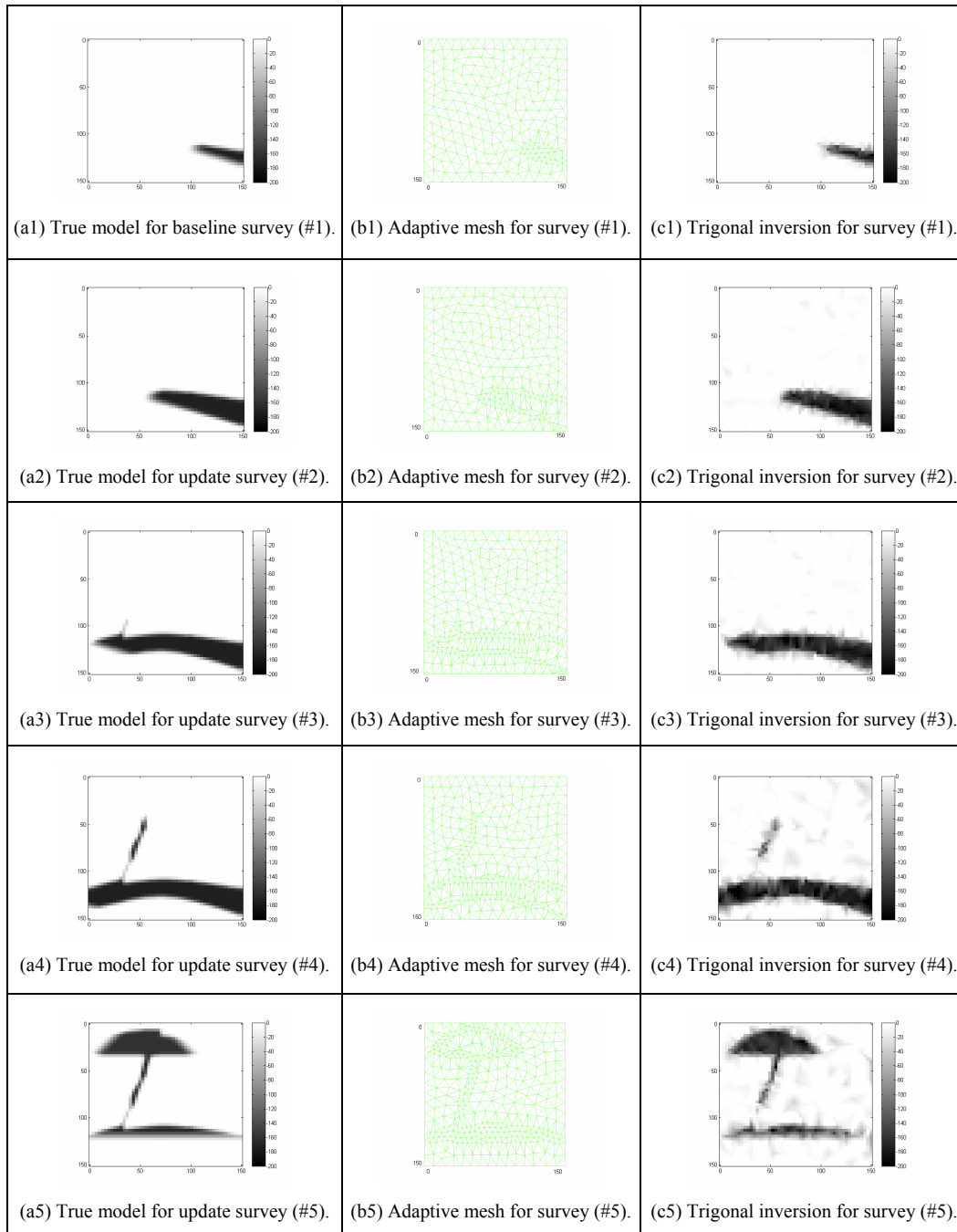


Figure 47: Monitoring test with adaptive triangular meshes. True models, adaptive meshes and reconstructions are shown in columns a, b and c, respectively. Distances are in meters and velocities in m/s.

Data Evolution and Model Evolution

As outlined in Figure 39, we plan to use sparse datasets to update the baseline model on a quasi-continuous basis. One problem with this concept is that sparse datasets often lead to undesirable image artifacts because the inversion problem is underdetermined. To

address this problem, we first reduced the number of unknown parameters in the inverse model, e.g., the adaptive mesh from the previous section. In this section, we add the additional features of data and model evolution or prediction in order to further reduce the requirements on the underdetermined inversion algorithm. The data (\mathbf{d}) here can be travel time, amplitude, the full seismic trace, or other seismic observables; seismic velocity, reflectivity or other subsurface parameters are the model (\mathbf{m}) to be estimated. This estimation problem can be formally expressed as

$$\mathbf{d} = G\mathbf{m} ,$$

where G is an operator relating model and data. The length of the data vector \mathbf{d} equals to N , the number of source-receiver pairs, data points or groups of data points. N should be large enough so that a proper inversion can be done.

Data \mathbf{d} and model \mathbf{m} are time-varying because of the CO₂ injection process. Assume that a large and complete dataset \mathbf{d}_{i-1} is obtained corresponding to model \mathbf{m}_{i-1} , i.e., the baseline survey. We have

$$\mathbf{d}_{i-1} = [d_{i-1}^{(1)} d_{i-1}^{(2)} \dots d_{i-1}^{(N-1)} d_{i-1}^{(N)}]^T .$$

For a true 4-D monitoring, data acquisition must be continuous or quasi-continuous. As the model changes from \mathbf{m}_{i-1} to \mathbf{m}_i , only partial new dataset (say, P records, $P \ll N$) $\Delta\mathbf{d}_i$ are collected:

$$\Delta\mathbf{d}_i = [d_i^{(1)} d_i^{(2)} \dots d_i^{(P)}]^T .$$

If we use $\Delta\mathbf{d}_i$ to invert \mathbf{m}_i as an underdetermined inverse problem, the quality of the resulting image would be very poor because of incompleteness of the data. As illustrated in Figure 40, we may use one of several different methods to estimate or evolve a complete dataset. This estimation problem is formally described as a merging of the old dataset with the new incremental dataset:

$$\mathbf{d}_i = \mathbf{d}_{i-1} \oplus \Delta\mathbf{d}_i = [\hat{d}_i^{(1)} \hat{d}_i^{(2)} \dots \hat{d}_i^{(N-1)} \hat{d}_i^{(N)}]^T , \quad (33)$$

where \oplus is an operator representing the data evolution algorithms and $\hat{d}_i^{(k)}$ is the data estimated with these evolution algorithms. The simplest approach to obtaining \mathbf{d}_i may be the replacement of data records 1,2, ..., P in \mathbf{d}_{i-1} by $\Delta\mathbf{d}_i$, that is

$$\mathbf{d}_i = \mathbf{d}_{i-1} \oplus \Delta\mathbf{d}_i = [d_i^{(1)} d_i^{(2)} \dots d_i^{(P)} \dots d_{i-1}^{(N-1)} d_{i-1}^{(N)}]^T .$$

Another method is to predict the missing data from data history giving

$$\mathbf{d}_i = \mathbf{d}_{i-1} \oplus \Delta \mathbf{d}_i = [d_i^{(1)} d_i^{(2)} \dots d_i^{(P)} \dots \hat{d}_i^{(N-1)} \hat{d}_i^{(N)}]^T,$$

where $\hat{\mathbf{d}}_i = A_{i-1} \mathbf{d}_{i-1}$ describes a prediction process such as extrapolation and “^” means that the value is estimated. Here A_{i-1} is a prediction operator.

A more advanced approach is to predict \mathbf{d}_i from history data and then update the predicted data with current observed data $\Delta \mathbf{d}_i$, which is defined as

$$\hat{\mathbf{d}}_i = P(\Delta \mathbf{d}_i | \mathbf{d}_1, \dots, \mathbf{d}_{i-1}).$$

The Kalman filter [14] is a classical algorithm for this recursive prediction-update procedure. Let $\hat{\mathbf{d}}_0$ be the initial dataset and $\hat{C}_0 = \text{cov}(\hat{\mathbf{d}}_0)$ be the initial prediction error covariance. Then we can recursively evolve the temporal datasets with Kalman filter described by

$$\begin{aligned} \hat{\mathbf{d}}_{k+1} &= A_k \hat{\mathbf{d}}_k + K_k (\mathbf{d}_k - \hat{\mathbf{d}}_k) \\ \hat{C}_{k+1} &= (A_k - K_k) \hat{C}_k (A_k - K_k)^T + Q_k + K_k R_k K_k^T, \\ K_k &= A_k \hat{C}_k (\hat{C}_k + R_k)^{-1} \end{aligned} \quad (34)$$

where K_k is Kalman gain, Q_k is process noise covariance, R_k is measurement noise covariance, and \mathbf{d}_i is observed data that may be obtained through Equation (33) in our case. We have found some practical problems (e.g., large matrix dimensions and lack of reliable estimates for the covariance matrixes) for applying this standard Kalman filter shown in Equation 34. We need to develop an adequate form of the Kalman filter for our special purpose of temporal seismic data evolution.

Similar to data evolution, we may also apply the recursive prediction-update procedure to model evolution, so that we can incorporate history models and flow simulation results for the subsurface imaging. For the model evolution we define this estimation problem as

$$\mathbf{m}_i^* = P(\mathbf{m}_i | \mathbf{d}_1, \dots, \mathbf{d}_i),$$

and implement it by the Kalman filter. First, we use the flow simulation, history data $(\mathbf{d}_1, \dots, \mathbf{d}_{i-1})$ and an initial model to predict the model recursively by

$$\begin{aligned} \hat{\mathbf{m}}_{k+1} &= F_k \mathbf{m}_k + K_k (\mathbf{d}_k - G_k \hat{\mathbf{m}}_k) \\ \hat{C}_{k+1} &= (F_k - K_k G_k) \hat{C}_k (F_k - K_k G_k)^T + Q_k + K_k R_k K_k^T, \\ K_k &= F_k \hat{C}_k G_k^T (G_k \hat{C}_k G_k^T + R_k)^{-1} \end{aligned} \quad (35)$$

where F_k is the model prediction operation defined by flow simulation. Second, we incorporate the predicted model $\hat{\mathbf{m}}_i$ from Equation 35 to update the model using current observation \mathbf{d}_i :

$$\begin{aligned}\mathbf{m}_i^* &= \hat{\mathbf{m}}_i + K_i(\mathbf{d}_i - G_i \hat{\mathbf{m}}_i) \\ \hat{C}_i &= (1 - K_i G_i) \hat{C}_i \\ K_i &= \hat{C}_i G_i^T (G_i \hat{C}_i G_i^T + R_i)^{-1}\end{aligned}$$

Data \mathbf{d}_i can be either time evolved or directly acquired.

We performed a seismic monitoring simulation using the Kalman filter for model evolution, i.e., without data evolution. The result of the simulation was poor, but showed why additional information and/or constraints are required. Here, we briefly summarize the results of this Kalman filter test. In that simulation test, the crosswell geometry was used for demonstration purposes. The finite difference simulation method was used to calculate the full seismic wave field. Figure 48 shows the baseline model and a common source gather of the simulated data. We created a total of 221 time-lapse models and chose four of them for this monitoring test. A complete crosswell survey was run first; then four incremental partial time-lapse surveys were simulated (see Figure 49a). Figure 49b shows the true velocity differences between time-lapse models and the baseline model. Figure 49c gives the inversion results of the velocity differences. Because only partial surveys are used for the recursive dynamic estimation, the reconstructed images are poor, though we can roughly identify the area saturated with CO₂. This test has shown that direct use of partial surveys would result in an underdetermined inversion. We must use the history data plus current partial data to evolve a full data set for the dynamic imaging.

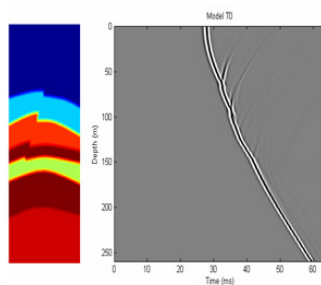


Figure 48: The geological model (left) and a common source gather of the simulated crosswell seismic data (right).

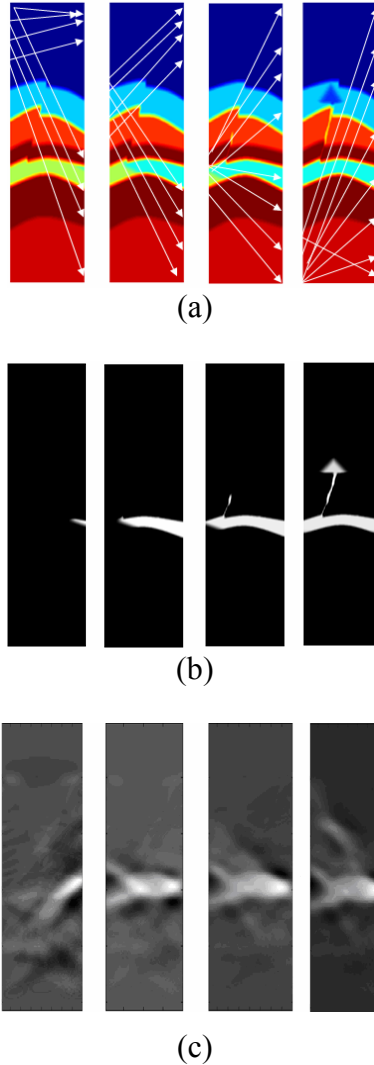


Figure 49: Kalman Filter tests. (a) Four partial surveys are collected as the model changes; (b) True model differences between time-lapse models and baseline model; (c) reconstructed velocity differences using Kalman filter for model evolution.

Summary

Our monitoring research has yielded results in three areas: (1) A data acquisition configuration that is unique for coal has been developed. This configuration incorporates circular surface arrays, shallow vertical arrays in one or more deep injection boreholes. (2) A fast image simulation procedure that allows us to quickly generate numerous idealized seismic images from time-lapse models. This procedure allows us to efficiently test data gathering and temporal integration strategies. (3) A unified inversion strategy for quasi-continuous monitoring using sparse incremental datasets. The strategy incorporates both data evolution and model evolution along with temporally adaptive and variable mesh that can be derived from flow predictions and model history. Our tests with Kalman filters yielded unexpectedly poor results, but we still believe Kalman filters will be useful when integrated with other methods, namely smart parameterization, and data evolution.

Future Work

The monitoring research is focused on quasi-continuous subsurface imaging. The major effort for the future falls in two categories: (1) implement and test the temporal integration strategy; (2) Test a “realistic” full simulation scenario of the quasi-continuous seismic imaging. The temporal integration strategy involves finding the optimal combination of data evolution, model evolution, and inversion algorithms that will permit quasi-continuous imaging from sparse datasets at reduced computational effort. The full simulation scenario involves using results from flow models, coal properties measured with DARS, and realistic seismic modeling and imaging methods to illustrate and assess the spatial and temporal resolution capabilities of the quasi-continuous monitoring strategy. An underlying task for all the monitoring research is to expand our existing 2-D numerical simulators to full 3-D. This effort may require some parallelization of the algorithms. An important though ancillary result will be the comparison of the fast technique for simulating an idealized image with the slow technique of simulating the more realistic image generated by modeling and inversion of the entire seismic acquisition and imaging process. If the former proves to produce accurate results under various conditions, we will have a fast way of quickly simulating monitoring strategies and storage/leak scenarios for 100’s of time-lapse models generated from flow simulations.

References

1. Shuck, E.L., T.L. and R.D. Benson, Multicomponent 3-D characterization of a coalbed methane reservoir: *Geophysics*, Vol. 61, No. 2, P. 315–330, 1996
2. Wang, Z., Seismic anisotropy in sedimentary rocks, part 2: Laboratory data: *Geophysics*, Vol. 67, No. 5, P. 1423–1440, 2002.
3. Buchanan, D. J., P. J. Jackson, and R. Davis, Attenuation and anisotropy of channel waves in coal seams: *Geophysics*, Vol. 18. No. 2, P. 13.1–147, 1983.
4. Dunne, J. and G. Beresfordz, Improving seismic data quality in the Gippsland Basin (Australia): *Geophysics*, Vol. 63, No. 5, P. 1496–1506, 1998.
5. Gochioco, L.M., Shallow VSP work in the U.S. Appalachian coal basin: *Geophysics*, VOL. 63, NO. 3, P. 795–799, 1998.
6. Henson, H., Jr. and J.L. Sexton, Premine study of shallow coal seams using high-resolution seismic reflection methods: *Geophysics*, Vol. 56. No. 9, P. 1494–1503, 1991.
7. Krey, Th., H. Arnetzb, and M. Knecht, Theoretical and practical aspects of absorption in the application of in-seam seismic coal exploration: *Geophysics*, Vol. 47., No. 12, P. 1645–1656, 1982.
8. Ramos , Antonio C. B. and Thomas L. Davisz, 3-D AVO analysis and modeling applied to fracture detection in coalbed methane reservoirs: *Geophysics*, Vol. 62, No. 6, P. 1683–1695, 1997.
9. Richardson S.E. and D.C. Lawton, Time-lapse seismic imaging of enhanced coalbed methane production: a numerical modelling study: *CREWES Research Report*, Vol. 14, 2002.
10. Akintunde, Olusoga M., Jerry M. Harris, and Youli Quean, 2004, Cross-well seismic monitoring of Coal Bed Methane (CBM) production: A case study from the Powder River Basin of Wyoming, *SEG Expanded Abstracts*, pp. 2307-2310.
11. Krail, P.M., Vertical cable as a subsalt imaging tool: *The Leading Edge*, Vol 13, 1994
12. Ikelle, L. and R.J. Wilson, Potential impacts of vertical cable (VC): *The Leading Edge*, Vol 18, 1999
13. J. S. Gulati, R. R. Stewart‡, and B. H. Hoffe, Vertical hydrophone cable acquisition and imaging on land: *Geophysics*, Vol 66, No. 4, P. 1190-1194, 2001
14. Maybeck, Peter S. 1979. *Stochastic Models, Estimation, and Control*, Volume 1, Academic Press, Inc.

15. Ajo-Franklin, J. B., J. A. Urban, and J. M. Harris, 2006, Using resolution-constrained adaptive meshes for travelttime tomography: *Journal of Seismic Exploration*, **14**, 371-392.
16. Ajo-Franklin, J. B., J. A. Urban, and J. M. Harris, 2005, Temporal integration of seismic travelttime tomography: 75th Annual International Meeting, SEG, Expanded Abstracts, 2468-2471.
17. Bottema, O., 1982, On the area of a triangle in barycentric coordinates: *Crux Mathematicorum*, **8**, 228-231.
18. Davis, T., M. R. B. Terrel, R. Cardona, R. Kendall, and R. Winarsky, 2003, Multicomponent seismic characterization and monitoring of the CO2 flood at Weyburn Field, Saskatchewan: *The Leading Edge*, **22**, 696-697.
19. Devaney, A. J., 1984, Geophysical diffraction tomography: *IEEE Transactions on Geoscience and Remote Sensing*, **22**, 3-13.
20. Harris, J. M., 1987, Diffraction tomography with discrete arrays of sources and receivers, *IEEE Transactions on Geoscience and Remote Sensing*, V. GE-25, n. 4, p. 448-455.
21. Lazaratos, S., and B. Marion, 1997, Crosswell seismic imaging of reservoir changes caused by CO2 injection: *The Leading Edge*, **16**, 1300-1306.
22. Lumley, D., 2001, Time-lapse seismic reservoir monitoring: *Geophysics*, **66**, 50-53.
23. Penrose, R., 1955, A generalized inverse for matrices: *Proceedings of the Cambridge Philosophical Society*, **51**, 406-413.
24. Persson, P.-O. and G. Strang, 2004, A Simple Mesh Generator in MATLAB: *SIAM Review*, **46**, p. 329-345.
25. Rickett, J., and D. Lumley, 2001, Cross-equalization data processing for time-lapse seismic reservoir monitoring: A case study from the Gulf of Mexico: *Geophysics*, **66**, 1015-1025.
26. Rocha Filho, A. A., 1997, *Formulação Matricial Multifrequência e Inversão Integrada* (in Portuguese): M.Sc. Dissertation, Federal University of Bahia.
27. Santos, E. T. F., 2006, *Inversão tomográfica sísmica anisotrópica com regularização ótima* (in Portuguese): D.Sc. Thesis, Federal University of Bahia.
28. Tikhonov, A. N., and V. Y. Arsenin, 1977, *Solution of Ill-Posed Problems*: Wiley.
29. Wu, R-S, and M. N. Toksöz, 1987, Diffraction tomography and multisource holography applied to seismic imaging. *Geophysics*, **52**, 11-25.